Green Chemistry

PAPER

View Article Online
View Journal | View Issue

Cite this: *Green Chem.*, 2026, **28**, 5033

Cu–N coordination-mediated H_2S absorption and controlled oxidation for efficient wet oxidative desulfurization

Zhihao Liu, [a] Renji Zheng[b] and Zhijie Chen *[c]

Received 26th November 2025,
Accepted 13th February 2026

DOI: 10.1039/d5gc06356f

rsc.li/greenchem

Conventional wet oxidative desulfurization suffers from the synchronous absorption–oxidation of H_2S, which induces sulfur deposition, viscosity rise, and equipment fouling. Here, we establish a stepwise "coordination capture-air regeneration" paradigm to achieve the absorption and controlled oxidation of H_2S. In this system, a Cu^{2+}–1-MI (1-methylimidazole)/DMF (*N*,*N*-dimethylformamide) solvent system selectively anchors H_2S through Cu–N coordination during absorption, while controlled air exposure regenerates the solvent and precipitates sulfur in a separate stage. The formulation achieves a breakthrough capacity of 14.3 g L^{-1} under ambient conditions, maintains ~95% capacity after multiple absorb–regenerate cycles, and shows good water tolerance. At the optimal Cu^{2+} : 1-MI ratio of 1 : 2, the liquid is near-neutral (pH ≈ 7.3) and induces relatively low corrosion 304L/316L stainless steels. The combination of experiments, characterization studies and density functional theory (DFT) calculations indicate that the Cu–N center captures and stores HS^- through coordination mechanisms, and achieves mild oxidation of HS^- by activating oxygen, while itself recovering. During absorption operated without external O_2 co-feeding, a small fraction of S–O species is detected, consistent with limited side oxidation attributable to dissolved oxygen. Overall, this "coordination anchoring–selective regeneration" concept mitigates rapid solid accumulation and suppresses over-oxidation of sulfur products, offering a promising basis for practical wellhead and high-pressure natural-gas purification.

Green foundation

1. We report a green, low-cost organic-phase desulfurization system that uses a coordination-anchoring mechanism to decouple sulfur uptake from oxidation, eliminating sulfur plugging common in wet oxidative desulfurization. As an economical alternative to ionic liquids and other emerging solvents, it offers markedly lower viscosity, corrosivity and energy demand and enables stable direct treatment of sour gas streams.
2. A simple formulation based on non-precious Cu salt and a low-volatility ligand in a recyclable polar solvent achieves high sulfur capacity (14.34 g L^{-1}), retains >80% capacity in water-rich media, exhibits negligible Cu leaching (<0.1%) and minimal corrosion, and delivers the lowest operating cost among benchmark regenerative solvents.
3. Greenness can be further advanced by replacing DMF with safer, ideally bio-based or water-rich media, lowering chloride content, intensifying solvent/ligand recycling, and extending coordination-fixation principles to benign metal–ligand pairs for distributed, low-carbon desulfurization.

1. Introduction

Wet oxidation desulfurization refers to a technology that uses a weakly alkaline solution to absorb H_2S from the gas and selectively oxidize it into elemental sulfur. The process is straightforward and achieves high purification, and is widely applied to small- and medium-scale streams (sulfur load < 5 t d^{-1});[1–4] representative implementations include the modified ADA process (Stretford process), Lo-CAT (complex iron method), and PDS (binuclear cobalt phthalocyanine sulfonate).[5–7] Nevertheless, widely employed wet desulfurization solutions still commonly suffer from issues such as high corrosivity, high viscosity, metal leaching, and limited sulfur capacity. More critically, most systems undergo redox reactions during the absorption stage, leading to the *in situ* generation of elemental sulfur (S^0) and some sulfur oxides within the absorber. Under high-pressure and high H_2S-flux conditions, intense localized supersaturation readily occurs at the gas–liquid interface, triggering rapid nucleation and aggregation.[8,9]

---

[a] *College of Environmental and Ecology, Chongqing University, Shapingba District, 401331 Chongqing, China*
[b] *School of Minerals Processing and Bioengineering, Central South University, Changsha 410083, China*
[c] *School of Civil and Environmental Engineering, The University of New South Wales, Sydney, NSW 2052, Australia. E-mail: zhijie.chen1@unsw.edu.au*

This results in the deposition of solid sulfur along flow paths, causing clogging and erosion of valves, nozzles, and mass-transfer internals. Simultaneously, sulfur colloids significantly increase the apparent viscosity of the slurry, which further elevates pressure drop and circulation energy consumption, while also accelerating the deactivation and irreversible loss of active components. Taking the conventional Lo-CAT process as an example (Fig. S1), the rapid accumulation of sulfur in the circulating liquid often leads to increased viscosity and pipeline blockage, substantially raising operational costs. Therefore, suppressing or mitigating the rate of solid formation during the absorption step to break the chain reaction of precipitation, viscosity increase, clogging and deactivation has become a critical scientific and engineering challenge for achieving safe and stable operation under wellhead conditions.[10–12]

Molecular design of the desulfurization liquid remains pivotal to process optimization. In recent years, ionic liquids (ILs) and deep eutectic solvents (DESs) have delivered advances in purification and emissions control relative to conventional Lo-CAT, yet three common challenges persist: (i) the high viscosity and acidity of many ILs severely hinder gas–liquid mass transfer, resulting in inefficient H_2S uptake and conversion; (ii) the coexistence of chloride anions and Lewis-acidic metal centers substantially elevates pitting risk for steel equipment; and (iii) most ILs rely on high pressure and high temperature to work effectively, leading to high operating costs, high safety risks, and poor performance under milder conditions. To address these issues, introducing a polar organic phase into the liquid has been shown to reduce acidity and viscosity while enhancing H_2S absorption.[13–15] For example, Yu and co-workers blended five organic solvents (DMF, DMAC, NMP, DMI, PEG200) into two chelated iron-based ILs to prepare BmimFeEDTA/solvent and BZKFeEDTA/solvent systems; the NMP, DMF, and DMAC formulations maintained ~97.5% desulfurization over 180 min. In addition, conjugated organic ligands can strengthen Fe(III) coordination, alleviate EDTA constraints on Fe(III), and thereby improve Fe(III)/Fe(II) cycling.[16] Nevertheless, existing IL/DES systems still face low sulfur capacity, poor stability, and slow, incomplete regeneration; loss of the metal active center further limits service life.[17]

To overcome these limitations, we propose a coordination-anchoring strategy that avoids generating large amounts of solid during the absorption stage *via* coordinated process- and molecular-level design. Specifically, the desulfurization liquid operates in the absorber under a low redox-potential window, where metal–ligand cooperation and solvent stabilization temporarily store HS^- as soluble, non-precipitating species, thereby preventing instantaneous sulfur formation during absorption. The rich liquid is then sent to a separate unit for controlled oxidation, releasing sulfur on demand and closing the regeneration loop of the coordination framework. In this work, DMF serves as the reaction medium; $CuCl_2$ is introduced, and 1-methylimidazole (1-MI) is employed as an N-donor ligand to enhance Cu^{2+} coordination stability and valence buffering, suppress irreversible CuS precipitation and instability under chloride/alkaline conditions, and – through polarity and viscosity tuning – improve HS^-/complex solubility and mass transfer while reducing corrosion and hydraulic losses (Fig. 1a and b). In practice, the concept is fully drop-in compatible with Lo-CAT hardware: existing absorber–regenerator–filtration modules can be retained, and only the desulfurization liquid formulation is replaced to avoid sulfur agglomeration and plugging. In the absorption tower, the supply of oxygen is unnecessary; H_2S is captured by Cu^{2+}–1-methylimidazole (1-MI) coordination in DMF, keeping the liquor clear and low-viscosity. The rich, particle-free solution is then pumped to the regenerator, where mild aeration drives stepwise oxidation to sulfur and enables easy solid–liquid separation, minimizing hydraulic losses and fouling risks. At the molecular level, DMF provides a low-viscosity, low-corrosion medium and enhances HS^-/complex solubility; $CuCl_2$ + 1-MI establishes robust Cu–N coordination and stabilizes performance under chloride/near-neutral conditions.[15,18] Experimentally, the Cu^{2+}–1-MI/DMF system delivers a sulfur capacity of 14.34 g L^{-1} at room temperature and maintains stable composition–performance over five reuse cycles. Deployed for small-footprint, high-pressure natural-gas desulfurization, the approach can simplify well-site operations and enable greener, more efficient, and more economical utilization of sour wellhead gas.

2. Experimental section

Materials and instruments

Details of materials and reagents can be found in the SI.

Preparation of desulfurization solution

A desulfurization system was prepared by dissolving an appropriate amount of copper chloride and chelating agent in 30 mL of DMF solvent. Then the two components are mixed and fully stirred to form a uniform desulfurization medium composed of miscible organic phases.

Desulfurization and regeneration tests

After preparation, the desulfurization solution was transferred into a bubbling reactor, and the desulfurization apparatus was assembled. The composition and schematic diagram of the desulfurization unit are shown in Fig. S2. Each desulfurization experiment uses 30 mL of desulfurization liquid, the concentration of H_2S in the feed gas is 50 000 ppm (5%), the default gas velocity is 40 mL min^{-1}, and the reaction temperature is 20 °C. During the desulfurization process, the outlet H_2S concentration was measured every 5 min. The breakthrough point was defined as the moment when the H_2S concentration in the outlet gas exceeded 20 ppm, at which point the experiment was terminated. The H_2S absorption capacity of the desulfurization agent was expressed in terms of sulfur capacity, which was calculated according to eqn (1):

$$a = \frac{Q \times \left(t_1 \times C - \int_{t_2}^{t_1 - t_2} C' \mathrm{d}t\right) \times M_{\mathrm{H_2S}}}{1000 \times V_{\mathrm{m}} \times V} \tag{1}$$

The sulfur capacity of the desulfurization agent, denoted as a (g L^{-1}), is calculated based on the following parameters: Q

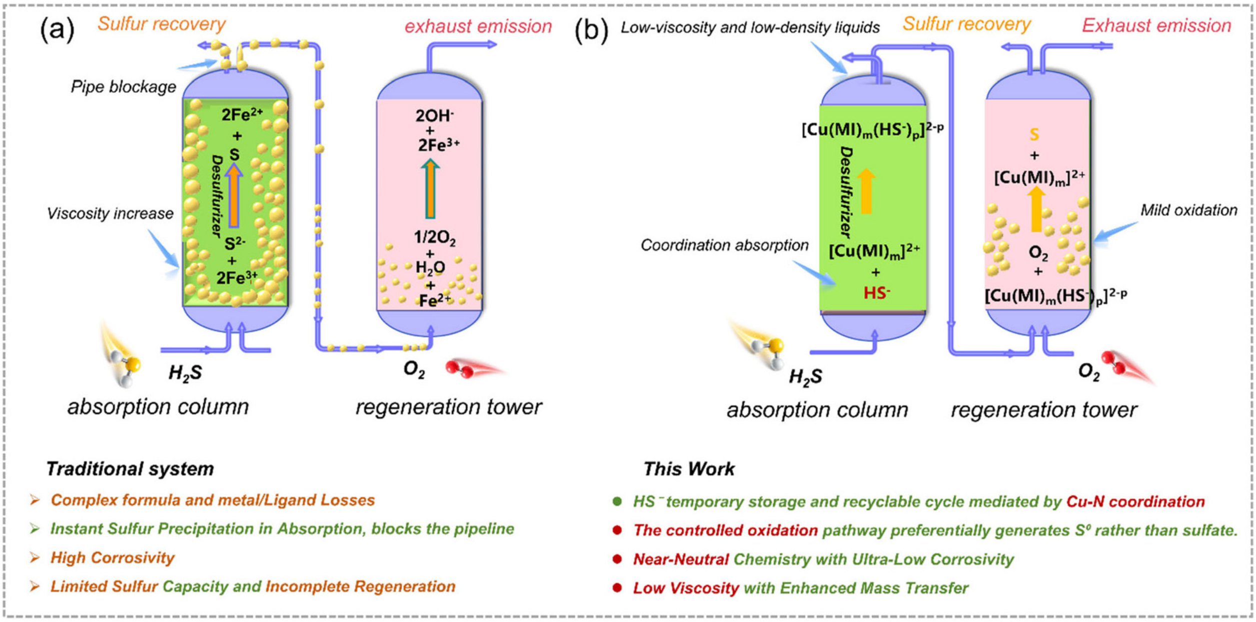

Fig. 1 Comparison between the absorption–oxidation spatial decoupling process and the traditional desulfurization system. (a) The traditional wet purification mechanism. (b) The purification mechanism of the coordination absorption–stepwise oxidation system as adopted in this study.

represents the inlet gas flow rate (mL min^{-1}); t_1 is the desulfurization time at which the H_2S concentration in the outlet gas first exceeds 20 ppm, marking the termination of the experiment (min); C is the H_2S concentration in the feed gas (%); t_2 denotes the breakthrough time, *i.e.*, the point when H_2S is first detected in the outlet gas (min); M_{H_2S} is the molar mass of H_2S (g mol^{-1}); V_m is the molar volume of gas (22.4 L mol^{-1}); and V is the volume of the desulfurization solution (mL). The outlet H_2S concentration (C') in this study did not exceed 20 ppm, which is negligible compared to C; therefore, in the integral term $\int_{t_2}^{t_1-t_2} C'\mathrm{d}t$, $C'\mathrm{d}t$ can be ignored without affecting the accuracy of the final result.

For the regeneration experiments, 40 mL of the spent desulfurization solution was placed into a U-shaped bubbling reactor. Pure oxygen was introduced at a flow rate of 200 mL min^{-1}, and the oxidation–reduction potential (ORP) of the solution was recorded every hour. The device for the regeneration test is shown in Fig. S3. After regeneration, elemental sulfur was separated from the liquid phase, and the regenerated solution was reused in subsequent desulfurization cycles. The purification efficiency was evaluated by plotting the outlet H_2S concentration as a function of desulfurization time. An extended desulfurization duration after regeneration was considered indicative of enhanced catalytic oxidation performance of the regenerated catalyst.

Details of the corrosion tests and computations can be found in the SI.

Corrosion experiment

The details of the corrosion experiment can be found in the SI.

Computational details

The details of the corrosion experiment can be found in the SI.

Techno-economic analysis

The capital data calculated for each item can be found with detailed information in the SI.

3. Results and discussion

Physical and chemical characteristics of the desulfurizer

To elucidate the nature and stability of the active Cu–1-methylimidazole (1-MI) complexes in DMF, we performed Fourier transform infrared (FT-IR) spectroscopy, thermogravimetric analysis (TGA) and density functional theory (DFT) (Fig. 2). In the FT-IR spectra (Fig. 2a), neat DMF exhibits a strong C═O stretch at 1660 cm^{-1}.[19,20] Upon adding $CuCl_2$, the 1660 cm^{-1} band remains essentially unchanged, while a new low-frequency feature appears near ∼700 cm^{-1}, consistent with a metal–ligand vibration (Cu–O in a DMF-bound species), indicating that Cu^{2+} coordinates to the carbonyl oxygen of DMF to form $[Cu(DMF)_n]^{2+}$-type adducts. Introducing 1-MI yields a new band at ∼622 cm^{-1}, attributable to the Cu–N vibration,[13,21] accompanied by the attenuation of the Cu–O feature. These sequential changes indicate ligand exchange from DMF-O to 1-MI-N, establishing a Cu–N coordination environment in the working solution and providing direct spectroscopic evidence for Cu–N complex formation.[22–25]

Thermogravimetry (Fig. 2b) shows a minor mass loss below ∼100 °C, assigned to solvent and weakly bound volatiles, followed by a major loss centered at ∼192 °C with a cumulative mass decrease of ∼93%, consistent with decomposition/evaporation of organic components (1-MI/DMF) and leaving a small inorganic residue.[14,15,26] Thus, the coordination species are stable in solution from room temperature up to at least

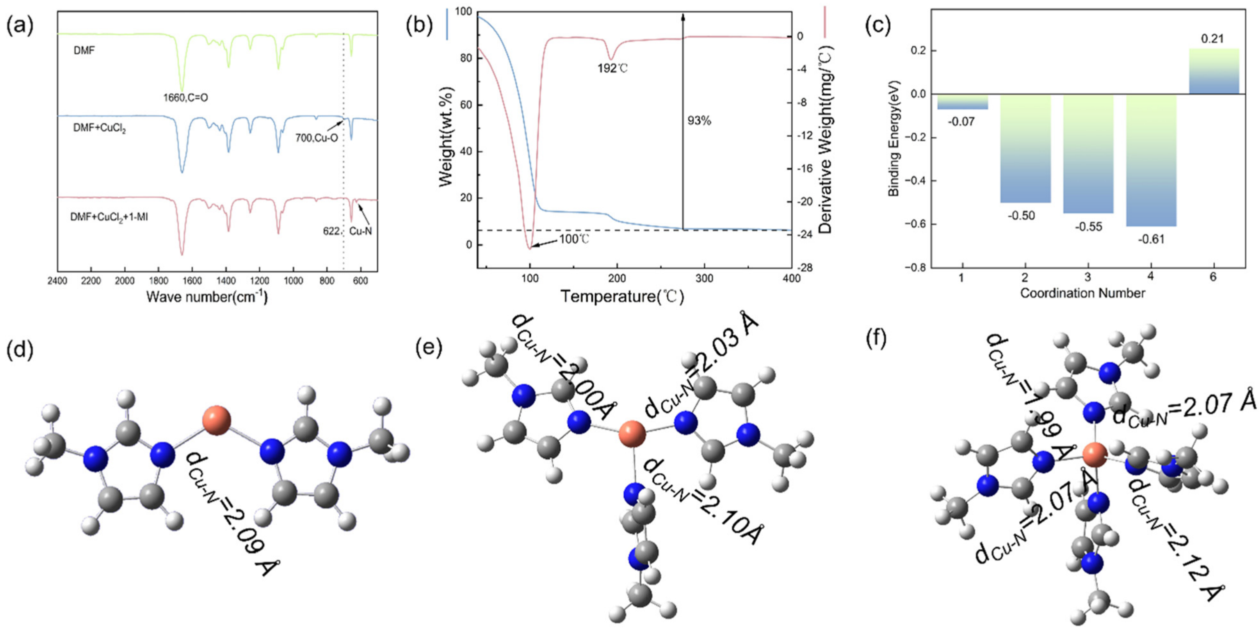

Fig. 2 Structure speculation of active components in the desulfurization solution. (a) FTIR spectrum. (b) Thermogravimetric spectrum. (c) Formation energy of Cu–methylimidazole molecular configurations with different coordination numbers in solution based on theoretical calculation and prediction. (d–f) Molecular configurations of di-, tri- and tetra-coordination and their key bond length data.

<60 °C, but at elevated temperatures or high sulfur loadings the organic ligands are removed and Cu converts to an inorganic phase. To ensure stable operation, the desulfurization solution should work at 60 °C. For engineering deployment, we evaluated key fluid properties: density and viscosity. As shown in Table S1, the density is only weakly temperature dependent but increases monotonically with 1-MI content. At $n(\mathrm{Cu}^{2+})$:n(1-MI) = 1 : 3, the density rise plateaus and blue flocculent precipitation appears upon standing in air (Fig. S4), indicating coordination saturation/aggregation of the Cu-ligand ensemble; accordingly, practical formulations should be limited to ≤1 : 2. Table S2 shows that the viscosity decreases slightly with temperature – implying modest thermal sensitivity – and increases moderately with higher Cu^{2+} : 1-MI ratios, yet remains substantially lower than typical ionic liquids or amine solvents.[19] The resulting low viscosity is favorable for gas–liquid mass transfer and process scale-up. To quantify coordination stability, we optimized geometries and computed single-point energies (Gaussian 09) for Cu^{2+} with varying numbers of 1-MI ligands (Fig. 2c–f). As the coordination number increases from 1 to 3–4, the Cu-ligand binding becomes progressively more favorable (from ∼−0.07 to −0.61 eV). At six-coordination, the binding switches to becoming endothermic (+0.21 eV), and the structure relaxes toward a four-coordinate core plus two detached ligands, indicating that over-coordination is thermodynamically disfavored. This trend is consistent with the electronic/structural preferences of Cu centers (Jahn–Teller elongation for d^9 Cu(II) in crowded octahedra and the soft-acid character of Cu(I)), whereby 2–4 coordination affords a more favorable balance of sterics and electronics.[27,28] Correspondingly, computed Cu–N bond lengths for 2–4 coordinate species cluster around 2.00–2.10 Å, indicating robust metal–ligand interactions and geometric stability.

Collectively, spectroscopy, thermal analysis and theory converge on a picture in which 2–4-coordinate Cu–N complexes (with four-coordinate being most stable) dominate in solution. This manifold provides both solution stability and sufficient site accessibility, enabling competitive coordination under desulfurization conditions.

Desulfurization performance

To systematically evaluate the purification performance of the desulfurization liquid, we examined the H_2S removal behavior of different solvent systems under a feed containing 50 000 ppm H_2S, as shown in Fig. 3. The breakthrough curves of the desulfurization solution under different components and reaction conditions are shown in Fig. S5. In the tests, the "effective purification time" was defined as the continuous period during which the outlet H_2S concentration remained below 20 ppm; the experiment was terminated when the outlet H_2S concentration reached 20 ppm (breakthrough concentration), and the resulting sulfur capacity was recorded as the breakthrough capacity. All desulfurization experiments were repeated three times to ensure usability.

The effect of different N-containing ligands on the purification capacity of the desulfurization liquid was investigated. In 30 mL of DMF, we dissolved 2 g of $CuCl_2$ (0.014 mol) and 2.46 g of 1-methylimidazole (1-MI, 0.028 mol) to construct a base desulfurization system. Different N-containing ligands

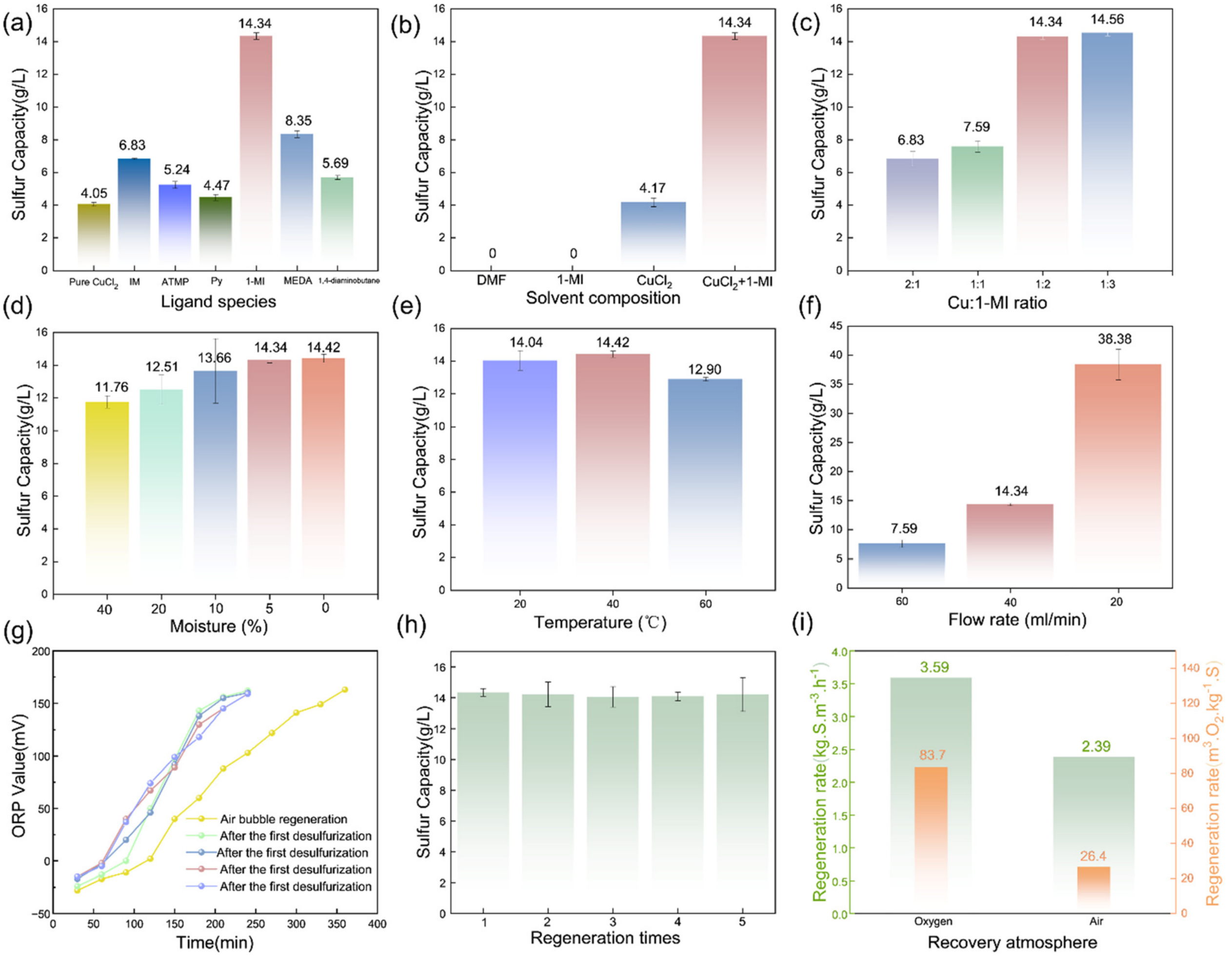

Fig. 3 Sulfur capacity of desulfurization solutions under different components and reaction conditions. (a) Type of ligands. (b) Composition of the solution. (c) Ratio of Cu to 1-MI. (d) Moisture content. (e) Reaction temperature. (f) Gas flow rate. (g) Variation of ORP values of the desulfurizer with regeneration time. (h) Variation trend of sulfur capacity of desulfurization solution with regeneration times. (i) Comparison of regeneration efficiency between air and pure oxygen.

were then added at a Cu^{2+} : ligand molar ratio of 1 : 2 to prepare a series of composite desulfurization agents. As observed in Fig. 3a and S5a, when $CuCl_2$ was used as the only active component, the breakthrough time was short and the sulfur capacity was limited; introducing typical N-ligands (pyridines, primary amines, secondary amines, diamines, *etc.*) improved performance to some extent, but 1-methylimidazole (1-MI) delivered the most significant enhancement, with a pronounced rightward shift of the breakthrough curve and a sulfur capacity far higher than that of other ligands. Compared with other ligands, the advantage of 1-MI can be attributed to the strong σ-donation and moderate π-interaction of the aromatic heterocyclic N, which enables stable formation of 2–4-coordinate Cu–N complexes in solution while retaining accessible sites for inner-sphere substitution with HS^-.[29,30] In contrast, although aliphatic amines/diamines can coordinate, they are more prone to excessive chelation or to forming looser outer-sphere coordination, making it difficult to balance stability and accessibility, and thus overall are inferior to 1-MI. In addition, the combined effects of macromolecular size, steric hindrance, and system solubility may also limit desulfurization activity.[15,23,24] At room temperature, the sulfur capacity of the Cu–1-MI/DMF system reached 14.34 g L^{-1}. Therefore, a DMF + $CuCl_2$ + 1-MI desulfurization formulation was used for subsequent experiments. The synergistic effect of the components was further demonstrated by control experiments. As shown in Fig. 3b and S5b, DMF or 1-MI alone exhibited almost no H_2S absorption, indicating that $CuCl_2$ is the true purification active center. $CuCl_2$ alone provided only limited capacity, whereas the synergy of $CuCl_2$ and 1-MI led to a leap in sulfur capacity (Fig. 3f), suggesting that stable coordination between Cu and the N-ligand is a prerequisite for efficient desulfurization. On this basis, the proportions of the components were further optimized (Fig. 3c and S5c). As the molar ratio of $CuCl_2$: 1-MI increased from 2 : 1 to 1 : 1 and then to 1 : 2, the breakthrough time and capacity improved markedly; a further increase to 1 : 3 brought only slight gains. The performance improvement arises, on the one hand, because the increased 1-MI raises the pH of the desulfurization liquid, enhancing its physical/chemical absorption; on the other hand, the accelerated formation and increased density of Cu–N sites favor H_2S uptake. Further increases in ligand amount slow performance gains, mainly due to limits set by the Cu coordination number and solubility. Considering both performance and stability, $n(CuCl_2):n(\text{1-MI}) = 1:2$ was selected as the optimal ratio. In addition, although the desulfurization tests identify the Cu–1-MI complex as the effective active component, the role of the solvent during operation remained uncertain. We therefore varied the solvent and performed desulfurization–regeneration tests (Fig. S6a and d). The desulfurization and regeneration capacities (Table S3) showed only minor differences among solvents, indicating that the solvent in the liquid contributes only through physical absorption of H_2S and does not participate in the Cu^{2+}–1-MI coordination-driven chemisorption of H_2S. During desulfurization and regeneration, small amounts of water are produced, and ambient moisture can also enter the desulfurization liquid with the gas stream, thereby affecting its desulfurization ability. Whether additional water helps to improve performance remains unclear. Therefore, desulfurization experiments were carried out with water contents of 0%, 5%, 10%, 20%, and 40%, respectively, and the results are shown in Fig. 3d and S5e. As the water content increased, the desulfurization ability gradually decreased but overall showed a gentle trend. The desulfurization times of the water-free liquid and the liquid containing 5% deionized water were roughly the same, indicating that the small amount of water introduced during operation has little effect on the desulfurization capacity. When the deionized water content increased to 40% of the liquid volume, the sulfur capacity remained at 11.76 g L^{-1}, which is 81.5% that of the completely dry sample, indicating good system stability. These results show that no additional water needs to be added; a DMF solution with $n(CuCl_2):n(\text{1-MI}) = 1:2$ affords the best desulfurization performance and can efficiently remove H_2S from high-concentration streams at room temperature.

CO_2 and H_2S are the dominant acidic impurities in the process gases, with comparable size and acidity, although CO_2 is typically present at orders-of-magnitude higher concentrations. Therefore, insufficient H_2S selectivity would promote CO_2 co-absorption, shortening liquor lifetime and wasting reagent. To assess selectivity under realistic conditions, we tested feeds where CO_2 greatly exceeded H_2S. Sulfur capacities with and without CO_2 were essentially identical (14.04 *vs.* 14.34 g L^{-1}; Fig. S6b and e), and the breakthrough curves nearly overlapped (Fig. S5e), diverging only slightly in the tail region. Thus, CO_2 uptake is dominated by physical dissolution with minimal interference, whereas selectivity stems from the affinity of the soft Lewis acid Cu^{2+} for HS^- in a near-neutral ligand field. This intrinsic selectivity underpins stable purification in CO_2-rich feeds. In addition, practical operating conditions that affect mass transfer and reaction are also important. Temperature experiments (Fig. 3e and S5d) show that the capacities are similar in the range of 20–40 °C, followed by a decrease at 60 °C. This trend is consistent with the increase of Henry's constant with temperature, which lowers H_2S solubility; continuous heating may also cause coordination instability, potentially reducing purification ability. The solubility effect outweighs the kinetic promotion by temperature, suggesting operation near room temperature to balance capacity and stability. Gas flow experiments (Fig. 3f and S5f) show that reducing the volumetric flow significantly prolongs the breakthrough time and increases capacity, indicating that under conventional conditions the system is mainly controlled by gas–liquid mass transfer/residence time; when the flow is reduced, Cu–N active centers in the liquid phase have more time to contact and capture H_2S molecules, resulting in a marked increase in sulfur capacity.[25,26] To accommodate variable throughputs, we optimized pressure within process and equipment limits. In principle, higher pressure raises the H_2S partial pressure and solubility, enhancing gas–liquid mass transfer; beyond a narrow window, however, it accelerates interfacial sulfur agglomeration and caking, increasing viscosity and causing localized plugging. With all other parameters fixed, we varied pressure from 1–3 bar (Fig. S6c and f). The capacity rose modestly from 1 to 2 bar, consistent with improved dissolution, whereas 3 bar yielded only an additional 0.17 g L^{-1}, indicating pronounced diminishing returns and proximity to dissolution/coordination saturation. Balancing performance against safety, energy consumption, and mechanical load, we recommend near-ambient operation ($\approx$1 bar) to sustain high conversion and overall process robustness and economics. Notably, the solution remained optically clear with no particulates, implying that Cu–N coordination suppresses Cu–S nucleation and mitigates viscosity rise and fouling at the source.[27–29]

The regeneration performance of the desulfurization liquid is a pivotal indicator determining its practical applicability. The ORP value of the solution during the oxygen supply process was monitored to evaluate the regeneration degree of the solution. In all cycles, the ORP rose rapidly from an initially low/slightly negative value and stabilized at approximately +180 mV within 150–200 min, with curves from different cycles nearly overlapping. This indicates that the solution sustained an oxidative environment across multiple cycles, without detectable loss in the reoxidation ability of O_2 toward the active center. It is worth noting that the regeneration process is carried out at a low temperature of 25 °C and lasts for 4 hours. This period of time is sufficient to fully restore the performance of the desulfurization solution.[32,33] Interestingly, while the use of air as the oxidant at a constant flow rate achieved a similar regeneration effect, it required a longer duration (approximately 6 h). Under these conditions, the regeneration efficiency was 2.39 kg S m^{-3} h^{-1}. When normalized to an equivalent O_2 basis, the oxidant supply required for pure O_2 regeneration was 83.7 m^3 O_2 Kg^{-1} S, whereas air regeneration required only 26.4 m^3 O_2 Kg^{-1} S (Fig. 3i). Furthermore, it should be emphasized that the oxidant dosage provided under vigorous aeration conditions (*i.e.*, the upper-bound value) represents the total O_2 supplied rather than the net O_2 consumption; quantifying actual O_2 consumption would require an analysis of the O_2 content in the exhaust gas. From a practical standpoint, the feasibility of air-based regeneration is noteworthy: although the kinetics is slower than that of pure oxygen, it circumvents the higher costs associated with oxygen supply, thereby offering a more economically attractive pathway for industrial scale-up. Consistently, the breakthrough capacity remained at ∼14 g L^{-1} after five regenerations (Fig. 3h), with minimal fluctuations as indicated by the error bars, demonstrating negligible capacity decay and good cycling stability. Compared with traditional liquid desulfurizers, this system does not require large amounts of $FeCl_3$ to assist regeneration; the single-metal system can be fully regenerated by oxygen sparging alone, evidencing excellent reusability. Notably, after desulfurization, a minute amount of black solid (∼10 mg after drying) appeared in the liquid (Fig. S7), likely due to trace CuS. After five cycles, ICP-OES analysis showed that the Cu content in the liquid differed from that of the fresh sample by only 0.18% (Fig. S8), implying very low loss of active Cu and preservation of the active centers.[13,25]

In summary, the Cu–1-MI/DMF desulfurization solution can effectively purify high-concentration H_2S under room temperature, normal pressure and general humidity conditions. The ligand effect of 1-MI, the appropriate ratio (1 : 2), low sensitivity to water, reasonable operating conditions (close to room temperature, moderately reduced flow rate), and good reusability all jointly determine its outstanding penetration ability and application potential.

Desulfurization and regeneration mechanism

To further clarify the mechanisms underlying the high desulfurization efficiency and ease of regeneration, we conducted a rigorous study combining experiments, spectroscopic characterization, and theoretical calculations.

To rationalize the mild oxidation behavior of the solvent toward H_2S, we discuss the results from three aspects: evolution of solid products, dissolved-oxygen (DO) dynamics, and radical evidence. XRD shows that the solid collected after desulfurization is dominated by characteristic reflections of copper sulfides (CuS/Cu_2S), while the regenerated solid matches well with α-S, indicating that the regeneration step preferentially yields elemental sulfur rather than continuously accumulating metal sulfides (Fig. 4a). Consistently, EDS quantification (Table S10) gives an S atomic fraction of ∼98.35% and a Cu atomic fraction of ∼1.65%, confirming that the regenerated solid is mainly sulfur with only trace Cu carryover.

XPS further resolves the surface-species distribution of solids at different stages. Cu 2p deconvolution reveals coexisting Cu^+/Cu^{2+} in all samples (Fig. S9 and S10), with their relative fractions varying with operating conditions, consistent with a side-redox process such as $2Cu^{2+} + S^{2-} \rightarrow 2Cu^+ + S$.[31,32] Notably, when H_2S and O_2 are continuously co-fed, almost no solid is formed after desulfurization, suggesting that O_2 accelerates sulfur conversion and mitigates metal deactivation. In samples richer in reduced sulfur ($S^{2-}/S_n^{\ 2-}$), Cu is shifted toward the reduced state, whereas regenerated solids show a higher Cu^{2+} fraction, implying that regeneration partially restores interfacial Cu species toward a recyclable coordination/valence distribution.[33,34] The persistence of discernible N 1s and Cl 2p signals after both desulfurization and regeneration (Fig. S12 and S13), together with their stage-dependent intensity/lineshape changes, indicates that not all Cu is irreversibly converted to CuS (Fig. S11); a substantial fraction remains in a coordinated environment. In the N 1s spectrum, components at 399–401 eV indicate that coordinated/protonated nitrogen in the 1-methylimidazole/DMF matrix is retained, with the lower-binding-energy component assigned to metal-coordinated N and the higher-binding-energy component to protonated/oxidized N. Importantly, in regenerated solids the Cu–N component (∼399–400 eV) becomes dominant again, suggesting that ligand protonation/substitution during desulfurization is at least partially reversible and that Cu–N coordination is re-established upon O_2 regeneration.[35,36]

Consistent with these assignments, the main S 2p features of post-desulfurization solids lie within 160–162.5 eV, indicating that the surface is primarily composed of sulfide species (Fig. 4b–d, and Fig. S14 and S15). The sulfate signal is plausibly associated with additional oxidation during desulfurization. In the O 1s spectrum (Fig. S12), the main peak near 532 eV and a shoulder near 531 eV can be assigned to the C═O oxygen in DMF and oxygen in surface hydroxyl/oxide or sulfate species, respectively, in agreement with the $SO_4^{\ 2-}$ component detected in the S 2p spectrum. Without external O_2 supply (direct H_2S feed, or H_2S feed after N_2 purging), reduced sulfur ($S^{2-}/S_n^{\ 2-}$) accounts for a larger fraction and Cu–S/copper sulfide components accumulate more readily, indicating that incoming sulfur is preferentially immobilized *via* strong interactions with Cu. In contrast, regeneration highlights the role of O_2: elemental sulfur (∼164 eV) increases markedly after O_2 regeneration. Moreover, O_2-involved conditions (especially $H_2S/N_2/O_2$ co-feeding or O_2 pre-aeration) more readily produce/enhance $SO_3^{\ 2-}/SO_4^{\ 2-}$ signals, whereas regenerated solids obtained after N_2 purging retain a higher fraction of residual $S^{2-}/S_n^{\ 2-}$. These trends suggest that moderate O_2 promotes conversion of reduced sulfur ($S^{2-}/S_n^{\ 2-}$) to S^0 and improves sulfur formation, while stronger O_2 availability increases the contribution from over-oxidation pathways leading to $SO_x^{\ 2-}$.

The DO profiles further reflect the extent of oxidation initiated by dissolved oxygen during absorption (Fig. 4e). Under O_2-free absorption, DO rapidly decreases to ∼0 during continuous H_2S feeding, indicating an oxygen-centered redox process, consistent with the sulfate detected in the solids; a control experiment with N_2 purging (and keeping the setup sealed) reduces DO to an extremely low level, confirming that the residual oxygen originates from dissolved oxygen in the solvent rather than from the feed gas. In addition, although O_2 pre-aeration increases the initial DO level, DO still decreases rapidly to a very low level as oxidation proceeds, indicating that the Cu–N center can capture O_2. Notably, under mixed H_2S/O_2 feeding, DO remains at a relatively high level, indicating that although oxidative side reactions occur during absorp-

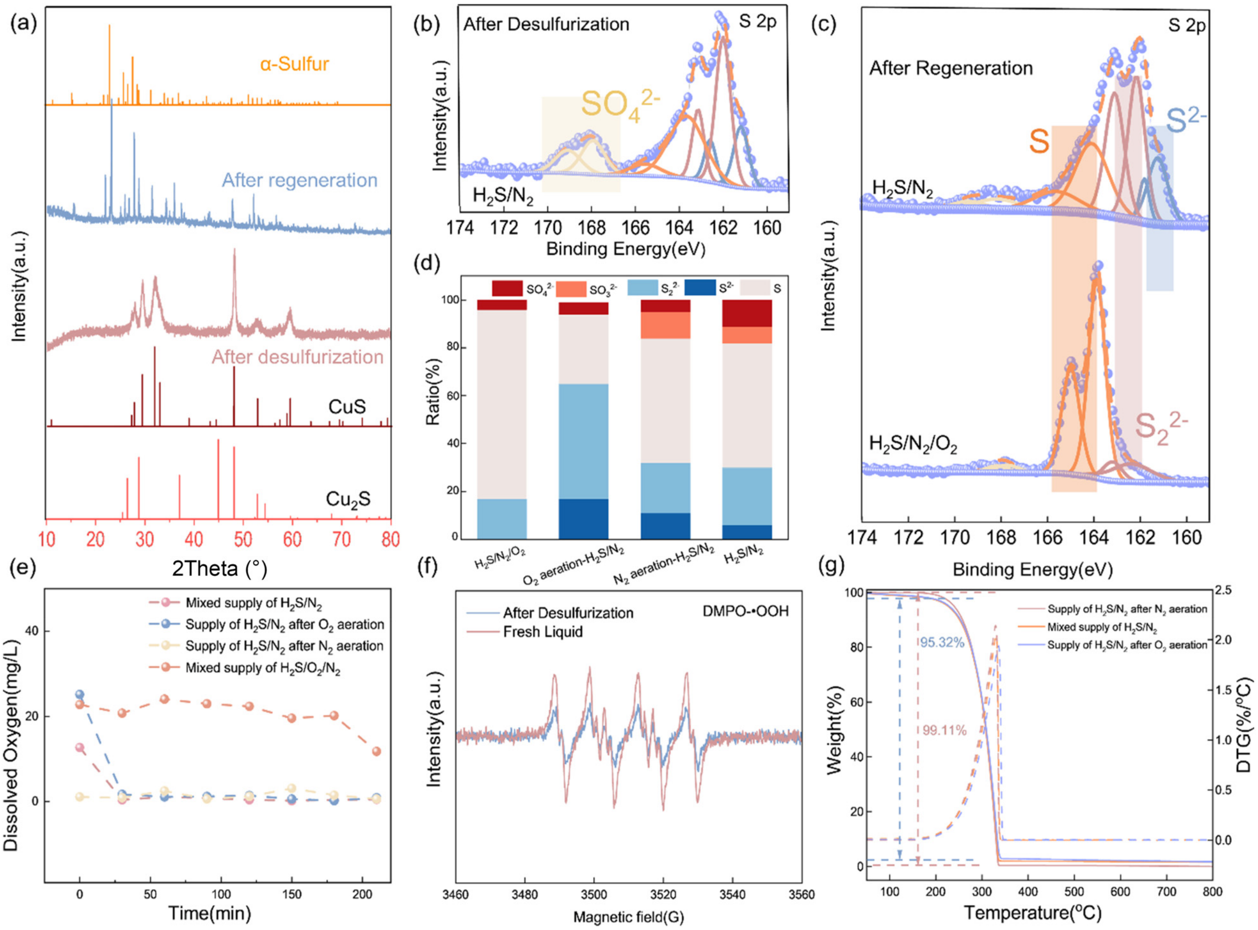

Fig. 4 Chemical evolution of catalyst during desulfurization and regeneration. (a) XRD spectra of the solid obtained at each stage. (b and c) XPS fine peak spectra of S elements in a small amount of solid after desulfurization and a large amount of solid components after regeneration. (d) Semi-quantitative proportions of each S substance in the solid produced under different operating conditions. (e) The trend of dissolved oxygen in the desulfurization liquid under different intake operation conditions. (f) The EPR test results of the desulfurization liquid. (g) Thermogravimetric curve of the regenerated solid.

tion, their extent is limited and cannot consume the continuously supplied O_2. The pH variation further supports this view: after N_2 pre-purging to remove dissolved oxygen, the solution remains weakly alkaline after desulfurization, whereas direct feeding or O_2 pre-aeration leads to a pH decrease, and continuous O_2 supply further aggravates it (Fig. S16). This indicates that over-oxidation gradually acidifies the solution, while without additional O_2 the acid–base state remains close to the initial level, showing good stability. These changes suggest that the absorption mechanism of this system is clearly different from traditional redox-dominated or simple acid–base neutralization pathways. EPR spin-trapping detects a DMPO-OOH signal, proving that the system can activate O_2 to form peroxide-related reactive species (Fig. 4f); more importantly, the fresh solution shows a stronger signal than the sulfur-loaded solution, indicating that O_2 activation is weakened under sulfur-rich conditions. This agrees with the observation that over-oxidation is suppressed: once HS^-/polysulfide species enter and become more strongly bound to the Cu–N center, the tendency for O_2 activation decreases, making it easier to keep oxidation within a milder range. The DFT trend is consistent: the HS^--induced CuN_2S_2 configuration binds and activates O_2 more weakly than the CuN_4 configuration (as reflected by its longer adsorption bond length and lower adsorption energy), providing molecular-level support for mild regeneration and limited over-oxidation (Fig. S17). Notably, the thermogravimetric curves, which reflect the overall composition, show nearly identical sulfur volatilization in the 150–350 °C range, with only a slight improvement in sulfur purity under conditions where dissolved oxygen is stringently removed (Fig. 4g).[37] This indicates that over-oxidation triggered by dissolved oxygen is more of a local/surface side reaction and its overall fraction is limited.

Overall, these results indicate that during absorption the dominant pathway is non-oxidative uptake (acid–base dissociation into sulfide species together with coordination anchoring to Cu), while oxidation caused by residual dissolved oxygen is only a secondary by-product route; fortunately, the oxygen content in most feed gases is extremely low (*e.g.*, natural gas and shale gas), so under practical conditions the absorption stage is expected to be only minimally affected by dissolved oxygen.

Detailed spectral characterization indicates that the absorption stage is mainly controlled by coordination chemical processes rather than the overall precipitation process. As shown in Fig. 5a, within the low-wavenumber region characteristic of metal–ligand vibrations, the spectrum of the H_2S-rich solution closely matches that of the freshly prepared solution, with no new bands observed, indicating that neither ligand framework underwent detectable chemical changes. Notably, the band at ~622 cm^{-1}, assigned to the Cu–N stretching mode, persists but shifts to lower wavenumber after desulfurization. This red shift implies a decrease in the Cu–N bond force constant and thus suggests that the introduction of H_2S perturbs the local

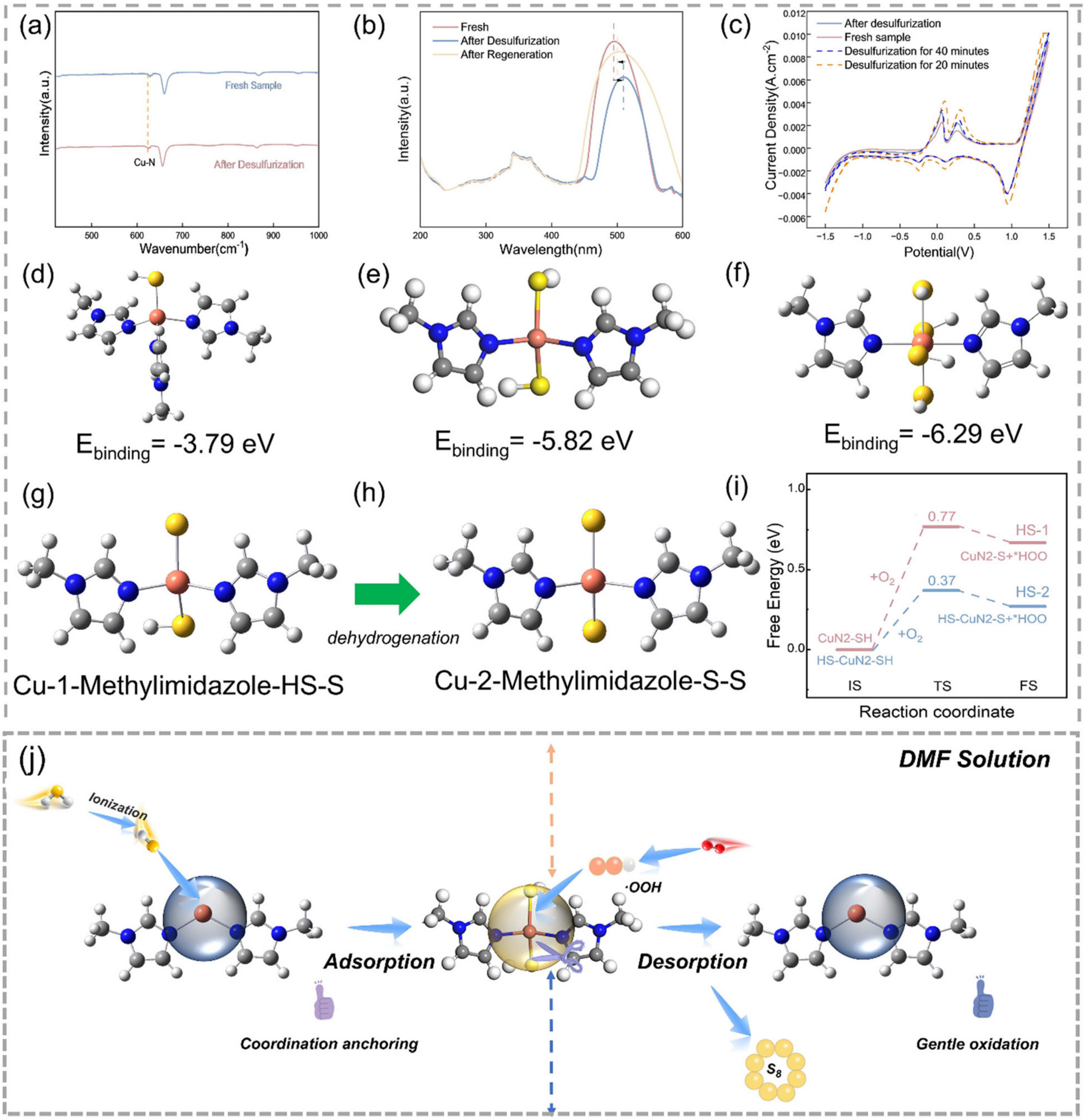

Fig. 5 Efficient removal of H_2S from desulfurization solution and its regeneration mechanism. (a) FTIR spectra of the Cu–MI system before and after desulfurization (b) UV-Vis spectra of the desulfurization solutions at each stage (c) CV curves of the Cu–MI/DMF system under different reaction times. (d–f) Adsorption configuration and binding energy of different coordinated Cu–1-MI molecules for HS^-. (g–h) Schematic diagrams of the dehydrogenation reaction structures of Cu-2N-2HS^- with O_2 participation. (i) Relative energy changes during dehydrogenation dissociation of Cu-2N-2HS^- with O_2 participation. (j) Suggested efficient desulfurization and regeneration mechanism.

coordination environment around Cu without disrupting the underlying Cu–N coordination scaffold. The UV-vis spectrum of the solution further confirmed this conclusion (Fig. 5b). It can be seen that during the desulfurization and regeneration processes, the main changes in the system are reversible alterations in the coordination of the metal center and the electronic structure, rather than the large-scale decomposition of the ligand framework: there are no significant changes in the three curves in the deep ultraviolet region (200–400 nm), suggesting that the main conjugated ligand framework is overall stable and the reaction is not mainly due to the destruction of the ligand structure. What is more indicative is the reversible change in the peak position of 450–550 nm (slightly raised after desulfurization and tending to fall back after regeneration), which is usually attributed to the superposition of sulfur-related absorption or the enhancement of ligand–metal charge transfer (LMCT) caused by sulfur participation in coordination.[38,39] Cyclic voltammetry further constrains the absorption chemistry. The fresh Cu^{2+}–MI/DMF solution displays a recognizable Cu^{2+}/Cu^{+} couple (near 0 V). Upon H_2S introduction (20–40 min), the Cu^{2+}/Cu^{+} peak currents decrease gradually, accompanied by a modest increase in peak separation, while the overall redox-feature shape remains discernible (Fig. 5c). This behavior is consistent with an EC-type scenario in which HS^-/S^{2-}, generated by H_2S dissociation in the basic medium, coordinates to the Cu center and reduces the fraction of freely diffusing electroactive Cu species, thereby attenuating current without eliminating the redox signature.[40] Importantly, the more negative reduction wave (assigned to $Cu^+ \rightarrow Cu^0$ in the MI-free case) is comparatively suppressed in the presence of MI, implying that ligand coordination disfavors pathways leading to metallic copper nucleation under the measurement conditions.[41–43] In contrast, the MI-free $CuCl_2$/DMF system shows much stronger current attenuation and peak broadening upon H_2S exposure, consistent with faster removal of Cu from the homogeneous phase (Fig. S18). Collectively, the FTIR/UV-vis/CV dataset supports MI stabilizing a coordinated Cu environment that can accommodate sulfide ligands during absorption, which mitigates rapid, irreversible loss of Cu into inactive solids.

To further resolve the molecular-level details of absorption–regeneration, we constructed Cu–$(1\text{-MI})_n$ (n = 2–4) active sites and examined the stepwise coordination of H_2S followed by dehydrogenation/oxidation (Fig. 5d). We first optimized the Cu–$(1\text{-MI})_2$–$2H_2S$ configuration involving direct H_2S adsorption. As shown in Fig. S19, the Cu–2N–$2H_2S$ structure is thermodynamically unstable: H atoms on the coordinated H_2S spontaneously migrate and bond to adjacent C atoms. This indicates that, when H_2S diffuses to the Cu–2N ligand surface, the combined action of basic surface sites on the ligand and solvent stabilization drives spontaneous dissociation to HS^-. Building on the foregoing experiments and characterizations, we compared HS^- binding under different coordination environments. The results show that CuN_2/CuN_3 adsorbs HS^- much more strongly than CuN_4 (Fig. 5e and f). In the free complex, CuN_4 (four-coordinate, approximately square-planar/elongated-octahedral) is most stable. However, this configuration is coordinatively saturated and sterically crowded, providing few available sites for HS^-; the barrier to adsorb the first HS^- already reaches 0.12 eV, implying it can scarcely proceed spontaneously. Furthermore, the gradual free energy change of the transformation of the CuN_4 species in the DMF solution to the sulfur-containing coordination configuration indicates that this step is thermodynamically feasible under the attack of HS^- (Fig. S20). Therefore, the actual adsorption process may be carried out by the low-coordination CuN_2 or CuN_3.

In the CuN_2 model, the total binding energy for the first two HS^- is −5.82 eV (Table S11), indicating substantial exothermicity and cooperative polarization. Upon introducing the third and fourth HS^-, the incremental binding is only −0.47 eV, indicating that the system approaches electrostatic saturation and subsequent coordination affords only marginal stabilization. Thus, although the overall energy of Cu–$(1\text{-MI})_2$–$4HS^-$ is lower, this is an additive effect of increased ligand/anion count rather than equally strong bonding for each HS^-. We therefore infer that Cu–$(1\text{-MI})_2$–$2HS^-$ is the dominant adsorption motif during desulfurization. Notably, the experimentally derived overall stoichiometry (≈1 mol S per mol Cu at breakthrough) indicates that the predominant sulfur uptake is effectively one sulfur equivalent per Cu at the process level, *i.e.*, the working inventory of sulfur stored per Cu is close to unity under the tested conditions. In this context, DFT models that accommodate two HS^- ligands on one Cu center should be interpreted as an upper-bound local motif that can become accessible in HS^--rich microenvironments (*e.g.*, near the gas–liquid interface), rather than as the dominant bulk speciation throughout the absorber.

In the absence of O_2, the ability to retain sulfur in a bound form is critical to the risk of sulfur loss from the rich solution. We therefore probed the facility of dehydrogenation for ligand-anchored HS^- without oxygen. As summarized in Table S11, without O_2 participation, the energy after H dissociation rises by 7.89 eV relative to the initial state, *i.e.*, it is highly unstable. This indicates that HS^- adsorbed at Cu–N sites cannot spontaneously dehydrogenate without oxygen.[41,44,45] Calculations on the Cu–2-methylimidazole–$4HS^-$ configuration likewise show that dissociation is unfavorable in the absence of O_2, indicating that ligand-anchored HS^- in the solvent is highly robust. Upon introducing O_2, the mechanism changes fundamentally. O_2 can adsorb *trans* to the copper center and become activated, forming an HS–Cu–O_2 motif. More importantly, once the first HS^- is dehydrogenated by the active oxygen and converted to H_2O + S*, the second HS^- dehydrogenates more readily (Fig. 6i) owing to reduced steric congestion and electronic redistribution, allowing two HS^- dehydrogenations to be completed within one cycle and thereby fully regenerating the adsorption site. Regarding products, Fig. S21 shows that oxidation of Cu–2-methylimidazole–$4HS^-$ tends to yield S_2/S_3 oligomers, which do not readily form the rhombic sulfur observed in product characterization studies; in contrast, dehydrogenation from Cu–2-methylimidazole–$2HS^-$ produces rhombic sulfur (Fig. 5g and h). This further indicates that,

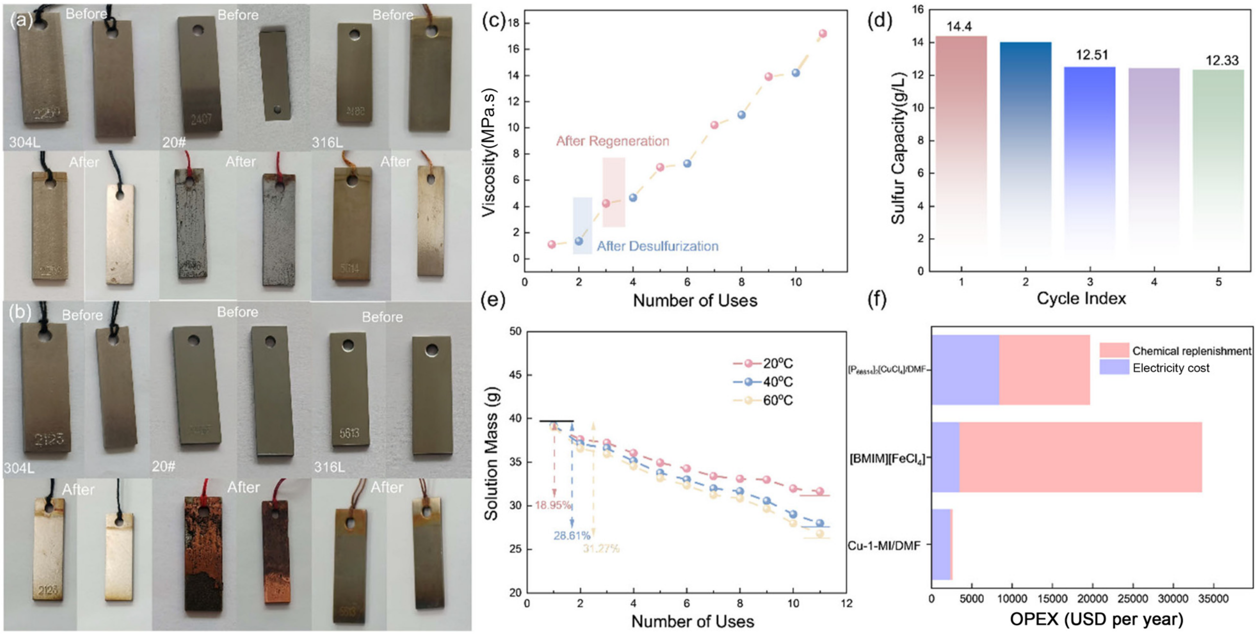

Fig. 6 Engineering feasibility analysis of desulfurization solution. The morphology of the stainless steel sheet before and after complete immersion (for 30 days) (from left to right: 304L, 20#, 316L stainless steel sheets): (a) moisture content 5%, (b) moisture content 20% (c–d) Changes in solution viscosity and corresponding sulfur capacity during the continuous desulfurization process (e) Recovery rate of the solution at different temperatures (f) Comparison of OPEX between the Cu–MI/DMF system and the conventional system under specified boundary conditions.

after desulfurization, the Cu–1-MI coordination center prefers the Cu–2-methylimidazole–2HS$^-$ complex rather than the Cu–2-methylimidazole–4HS$^-$ configuration.[46–48]

Based on these results, we propose the following absorption–regeneration picture for the Cu–1-MI/DMF system (Fig. 5j). In DMF, H_2S dissociates to HS$^-$, and 1-methylimidazole (1-MI) coordinates $CuCl_2$ to form a Cu–N environment. HS$^-$ is then preferentially retained *via* inner-sphere coordination at accessible Cu–N motifs, giving bound sulfide species in solution and keeping most sulfur in a non-precipitating form during absorption. During regeneration, introducing O_2 enables oxidative conversion of the stored sulfide toward S^0 while restoring the Cu–N site state, and sulfur is released as a separable solid.[49,50] Overall, the performance derives from the combined roles of (i) DMF as a low-viscosity medium that facilitates mass transfer and sulfide solvation, (ii) 1-MI coordination that stabilizes Cu centers and mitigates irreversible sulfidation, and (iii) the unique coordination anchoring effect of the Cu–N center and the HS$^-$.

Engineering feasibility analysis

To evaluate the engineering feasibility of this system, we assess four aspects—corrosion compatibility, cyclic stability, solvent recoverability, and a bounded operating-cost analysis (Fig. 6). First, the solution acidity/basicity was examined. With increasing 1-MI content, the liquid shifts from weak acidity to weak alkalinity (Fig. S22); at a $Cu^{2+}:$1-MI molar ratio of 1 : 2, the pH approaches neutrality (7.32), which lowers the risk of equipment and pipeline corrosion while favoring the initial dissociation and uptake of H_2S in the liquid phase.[51,52] Using this optimal formulation ($n(CuCl_2):n$(1-MI)=1 : 2), corrosion coupon tests were performed on two commonly used stainless steel materials (304L and 316L) (Fig. 6a, b and S23–S26; Tables S4–S8). Without additional water, the metallic luster of the coupons was largely preserved, with no evident discoloration, pitting, or lamellar spallation. As the water content increased, the 304L/316L still exhibited generally good corrosion resistance, whereas 20# carbon steel showed pronounced rusting that intensified with higher water content. Weight-loss-derived average corrosion rates indicate that when the water content increased from 5% to 20%, the corrosion rates of 304L and 316L rose from 0.0036 and 0.0026 mm per annum to 0.0048 and 0.0032 mm per annum, respectively, remaining at a low level; however, under continuous O_2 purging, more obvious surface discoloration and corrosion-product deposits were observed, suggesting that oxygen-rich conditions can amplify corrosion risk (Fig. S27). As a control, the Cu–DMF system exhibited more severe corrosion (Fig. S28 and Table S5), implying that the milder acid–base environment and coordination chemistry introduced by 1-MI help mitigate corrosion. Considering the formulation, trace Cl$^-$ derived from $CuCl_2$ is a potential risk factor: its high penetrability and competitive adsorption may locally weaken the passive film and induce mild pitting tendencies.[51,53,54] Therefore, further risk reduction during scale-up will still require appropriate materials selection and operating-window control, especially with respect to oxygen and water boundaries.

Second, to evaluate how viscosity changes during repeated operation influence mass transfer and performance, consecutive "desulfurization–regeneration" cycles were conducted, and viscosity evolution was tracked without filtering out solids. The viscosity increased cumulatively after desulfurization, from 1.69 mPa s for the fresh solution to 17.2 mPa s after five cycles. This growth is due to the accumulation of unseparated solid sulfur and other sulfur-containing substances. Despite the viscosity rise, the purification performance remained within an acceptable range: after five cycles, the sulfur capacity was ~12.5 g L^{-1}, corresponding to ~85.7% of the initial value (Fig. 6c and d). This indicates that, under the present experimental boundaries, the intrinsically low viscosity of DMF provides partial "buffering" against rheological changes induced by sulfur-product accumulation, thereby attenuating the impact of viscosity growth on short-cycle performance.[12,55,56]

Industrial deployment requires closed-loop solvent recovery; accordingly, we evaluated laboratory-scale recovery–reuse (Fig. 6e). The solution mass decreased progressively upon repeated operations, and the cumulative loss increased with temperature: solvent losses of 18.95%, 28.61%, and 31.27% were observed at different temperatures. These data show that, although DMF is relatively inexpensive and amenable to recycling, solvent loss is non-negligible in sustainability assessment and techno-economic accounting; moreover, the toxicity and environmental footprint of DMF should be treated as practical engineering constraints. On this basis, we carried out preliminary tests of alternative solvents (NMP and DMPO; Fig. S3). Compared with the uncoordinated systems, both alternatives showed substantial improvements, but their overall performance remained slightly inferior to DMF. Systematic solvent substitution guided by green metrics (toxicity, safety, recovery efficiency, *etc.*) will be pursued in future optimization.

Finally, to enable transparent and comparable economic discussion, we conducted a bounded OPEX benchmark for representative wet oxidative desulfurization solvents under unified boundary conditions (2160 Nm^3 per h feed, 5000 ppmv H_2S, 7200 h per year; Fig. 6f and Table S9). Because reliable data for several key cost items are not yet available at this stage, the analysis includes only directly quantifiable contributions—electricity consumption and chemical replenishment/working-fluid make-up—and explicitly excludes solvent degradation and long-term loss, sulfur-product purification, solids separation and handling, wastewater/waste treatment, and corrosion-related maintenance and materials-of-construction costs. Therefore, the results should be interpreted as a "bounded OPEX comparison" rather than a full process TEA. Within this defined scope, Cu–1-MI/DMF shows the lowest annual OPEX (2.56×10^3 USD per year; 0.022 USD per kg H_2S), primarily due to low chemical replenishment cost and low electricity demand. $[P_{66614}]_2[CuCl_4]$/DMF exhibits a higher OPEX (3.36×10^4 USD per year; 0.166 USD per kg H_2S), dominated by the high cost of the phosphonium–copper component, while [BMIM][$FeCl_4$] lies in between (1.95×10^4 USD per year; 0.284 USD per kg H_2S) and requires higher electricity input.

Overall, the engineering assessments and bounded economic comparison collectively indicate that, under a near-neutral, easily regenerated, and low-viscosity formulation, Cu–1-MI/DMF offers potential advantages for scale-up in terms of materials compatibility, short-cycle operational stability, and solvent/utility-dominated OPEX, while its long-term sustainability still requires more comprehensive process-level evaluation incorporating solvent loss, product purification, and solids/waste handling.

4. Conclusion

In conclusion, we demonstrate a stepwise "coordination capture–air regeneration" process using a Cu^{2+}–1-MI/DMF solvent for wet removal of high-H_2S gas streams. At ambient temperature and 50 000 ppmv H_2S, the formulation delivers a breakthrough sulfur capacity of 14.34 g L^{-1} and retains 11.76 g L^{-1} in the presence of 40 vol% water. With the optimized composition ($n(Cu^{2+}) : n(\text{1-MI})=1:2$), the solution remains near neutral (pH ≈ 7.3) and maintains ~95% of its capacity after five desulfurization–regeneration cycles, supporting its short-cycle operability. Mechanistic evidence from spectroscopy and DFT consistently indicates that H_2S uptake is dominated by Cu–N-assisted coordination, while oxygen is mainly involved in the regeneration stage; dissolved oxygen can trigger limited oxidation side reactions during absorption, reflected by trace S–O species, but multiple characterization studies indicate that the extent of over-oxidation is low under the tested conditions. Importantly, separating regeneration from absorption minimizes rapid solid accumulation during uptake and allows sulfur to be produced predominantly in the regeneration step. A screening-level, bounded OPEX comparison under unified assumptions (electricity and chemical make-up only) suggests that Cu–1-MI/DMF has lower solvent- and utility-related operating costs than the representative ionic-liquid redox solvents evaluated here; however, this comparison does not include several process-relevant items (*e.g.*, solvent degradation/loss, sulfur purification, solids handling, waste treatment, and corrosion-related maintenance), which should be addressed in future process-level analyses. Overall, this work provides an experimentally supported basis for designing coordination-based absorbents. Future efforts may focus on fine-tuning ligand structures (steric/electronic effects), strengthening solvent-mediated mass transfer, and defining regeneration boundaries (avoiding over-oxidation) to further increase throughput and extend run length.

Author contributions

Zhihao Liu: data analysis, methodology, writing – original draft, writing – review & editing. Renji Zheng: resources, supervision, funding acquisition, writing – review & editing. Zhijie Chen: resources, supervision, data analysis, writing – review & editing, project administration.

Conflicts of interest

There are no conflicts to declare.

Data availability

The data supporting this article have been included as part of the supplementary information (SI). Supplementary information is available. See DOI: https://doi.org/10.1039/d5gc06356f.

Acknowledgements

This study was supported by the National Natural Science Foundation of China (52204300), the 2024 Graduate Student Research Innovation Project of Chongqing (CYB240041), the National Key R&D Program of China (2024YFC2909600) and the Scientific Research Project of Hunan Provincial Department of Education (24B0024).

References

1 P. Wu, B. Wang, L. Chen, J. Zhu, N. Yang, L. Zhu, C. Deng, M. Hua, W. Zhu and C. Xu, *Adv. Sci.*, 2024, **11**, 2401996.
2 P. Wu, S. Ma and W. Zhu, *Green Chem.*, 2026, **28**, 37–95.
3 P. Wu, S. Ma, S. Zhou, Y. Sun, L. Chen, J. Liu, W. Zhu and C. Xu, *Chem. Eng. Sci.*, 2025, **305**, 121136.
4 P. Wu, B. Wang, H. Li, S. Ma, L. Chen, J. Liu, Y. Chao, W. Zhu and C. Xu, *AIChE J.*, 2025, **71**, e18739.
5 Y. Wang, X. Liu, A. Kraslawski, J. Gao and P. Cui, *J. Cleaner Prod.*, 2019, **213**, 480–490.
6 X. Liang, S. Chen, Y. Liang, M. Wang, Q. Wang, D. Chen, X. Ma, H. Ding and H.-J. Zhong, *Gels*, 2026, **12**, 182.
7 X. Zheng, G. Lei, S. Wang, L. Shen, Y. Zhan and L. Jiang, *ACS Catal.*, 2023, **13**, 11723–11752.
8 F. Gao, J. Li, C. Yang, W. Zhang, H. Huang, Z. Peng and T. Gong, *Nat. Gas Ind. B*, 2025, **12**, 26–36.
9 Z. Liu, K. Qiu, G. Sun, Y. Ma, Y. Wang, J. Peng, S. Chen and X. Song, *Res. Chem. Intermed.*, 2023, **49**, 701–716.
10 Z. Liu, G. Sun, Z. Chen, Y. Ma, K. Qiu, M. Li and B.-J. Ni, *J. Hazard. Mater.*, 2023, **450**, 131084.
11 K. Qiu, Z. Liu, Y. Dong, L. Liu, W. Li, S. Niu and Z. Jin, *Chem. Eng. Technol.*, 2022, **45**, 1867–1875.
12 F. Li, X. Xu, C. Cao, Z. Yang, G. Wang, T. Li, Y. Pu, S. Zhang, Z. Cheng, G. Lv, C. Xu, J. Xian, Y. Yang and Z. Pu, *J. Cleaner Prod.*, 2023, **397**, 136608.
13 L. Chen, R. Zhang, Z. Liu, W. Sun, F. Li, Z. Shen and W. Liu, *Environ. Sci. Technol.*, 2025, **59**, 21365–21378.
14 S. Gao, X. Chen, X. Xi, M. Abro, W. Afzal, R. Abro and G. Yu, *ACS Sustainable Chem. Eng.*, 2019, **7**, 5660–5668.
15 Y. Zhang, H. Ran, X. Liu, X. Zhang, J. Yin, J. Zhang, J. He, H. Li and H. Li, *Sep. Purif. Technol.*, 2023, **318**, 123963.
16 W. Bai, J. Chen, F. Liu, Z. Gu, Y. Zhong and J. Yu, *Process Saf. Environ. Prot.*, 2024, **189**, 813–827.
17 W. Bai, Z. Gu, Y. Zhong and J. Yu, *Sep. Purif. Technol.*, 2025, **359**, 130591.
18 C. Lv, Y. Cao, Y. Feng, L. Fan, J. Zhang, Y. Song, H. Liu and G. Gao, *Adv. Energy Mater.*, 2025, e05978.
19 Z. Liu, Z. Chen, D. Zhang and B.-J. Ni, *Environ. Sci. Pollut. Res.*, 2023, **31**, 2243–2257.
20 D. Luo, F. Zhao, Q. Wang, L. Liu, X. Chen, Y. Li and B. Dai, *Ind. Eng. Chem. Res.*, 2023, **62**, 19547–19558.
21 J. Vollertsen, A. H. Nielsen, H. S. Jensen, T. Wium-Andersen and T. Hvitved-Jacobsen, *Sci. Total Environ.*, 2008, **394**, 162–170.
22 Z. Zhao, T. Meng, R. Tang, J. Cai, Z. He, W. Wen and M. Cao, *Adv. Mater.*, 2026, e72365.
23 J. Huang, X. He, S. Zou, K. Ling, H. Zhu, Q. Jiang, Y. Zhang, Z. Feng, P. Wang, X. Duan, H. Liao, Z. Yuan, Y. Liu and J. Tan, *Biosensors*, 2025, **15**, 664.
24 J. Liu, S. Du, Z. Huang, N. Liu, Z. Shao, N. Qin, Y. Wang, H. Wang, Z. Ni and L. Yang, *Materials*, 2025, **18**, 2976.
25 J. Zhao, Z. Guo, T. Qi, Q. Lu, S. Chen, J. Wang, M. Feng, C. Sun and J. Ming, *Angew. Chem., Int. Ed.*, 2026, e19122.
26 V. Garcia-Arriaga, J. Alvarez-Ramirez, M. Amaya and E. Sosa, *Corros. Sci.*, 2010, **52**, 2268–2279.
27 J. Zhang and Z. Tong, *Chin. J. Chem. Eng.*, 2006, **14**, 810–813.
28 X. Zhang, W. Xiong, L. Peng, Y. Wu and X. Hu, *AIChE J.*, 2020, **66**, e16936.
29 X. Liang, B. Yu, Y. Dai, Y. Wang, M. Hu, H.-J. Zhong and J. He, *Materials*, 2025, **18**, 2202.
30 B. Chen, L. Wang, Y. Xiao, F. R. Fronczek, M. Xue, Y. Cui and G. Qian, *Angew. Chem., Int. Ed.*, 2009, **48**, 500–503.
31 S. Cai, B. Chen, X. Qiu, J. Li, P. G. Tratnyek and F. He, *Environ. Sci. Technol.*, 2021, **55**, 645–654.
32 Y. Xie, A. Riedinger, M. Prato, A. Casu, A. Genovese, P. Guardia, S. Sottini, C. Sangregorio, K. Miszta, S. Ghosh, T. Pellegrino and L. Manna, *J. Am. Chem. Soc.*, 2013, **135**, 17630–17637.
33 O. A. Habeeb, R. Kanthasamy, G. A. M. Ali, S. Sethupathi and R. B. M. Yunus, *Rev. Chem. Eng.*, 2018, **34**, 837–854.
34 J. H. Yang, *Korean J. Chem. Eng.*, 2021, **38**, 674–691.
35 A. V. Marenich, C. J. Cramer and D. G. Truhlar, *J. Phys. Chem. B*, 2009, **113**, 6378–6396.
36 J. C. F. Diogo, F. J. P. Caetano, J. M. N. A. Fareleira and W. A. Wakeham, *Fluid Phase Equilib.*, 2013, **353**, 76–86.
37 C. Sun, J. Zhu, B. Liu, M. Xu, J. Jiang and T. Yu, *ACS Energy Lett.*, 2023, **8**, 772–779.
38 X. Zhang, W. Xiong, M. Shi, Y. Wu and X. Hu, *Chem. Eng. J.*, 2021, **408**, 127866.
39 N. Wang, H. Chen, Z. Liu, Y. Wang, J. Jian, B. Wen, Y. Chen, Y. Liu, X. Wang and K. Qiu, *Chem. Eng. Technol.*, 2024, **47**, 851–855.
40 R. Gulaboski and V. Mirceski, *Electrochim. Acta*, 2015, **167**, 219–225.
41 J. Zhang, Y. Dong, D. M. Frangopol, S. Zhu and H. Yang, *Appl. Energy*, 2026, **408**, 127424.
42 A. C. Tella, V. T. Olayemi, F. A. Adekola, A. C. Oladipo, V. O. Adimula, J. O. Ogar, E. C. Hosten, A. S. Ogunlaja, S. P. Argent and R. Mokaya, *Inorg. Chim. Acta*, 2021, **515**, 120048.

43 B. Dede, N. Özen and G. Görgülü, *J. Mol. Struct.*, 2018, **1163**, 357–367.

44 F. Li, A. Laaksonen, X. Zhang and X. Ji, *Ind. Eng. Chem. Res.*, 2022, **61**, 2643–2671.

45 Z. Liu, K. Qiu, Y. Dong, Z. Jin, L. Liu and J. Wu, *Korean J. Chem. Eng.*, 2022, **39**, 3305–3314.

46 L. Lubian, R. Rubio-Presa, V. Ruiz, A. Colina and E. Ventosa, *J. Power Sources*, 2025, **646**, 237272.

47 Z. Liu, Z. Chen, Z. Wang, D. Zhang and B.-J. Ni, *Environ. Sci.: Nano*, 2024, **11**, 1394–1411.

48 M. Sun, X. Wang, Z. Zhao and J. Qiu, *New Carbon Mater.*, 2022, **37**, 675–694.

49 M. Tian, Y. He, G. Zhang and H. Wang, *Molecules*, 2022, **27**, 5964.

50 H. Zhao and G. A. Baker, *Front. Chem. Sci. Eng.*, 2015, **9**, 262–279.

51 G. Hua, Q. Zhang, D. McManus, A. M. Z. Slawin and J. D. Woollins, *Dalton Trans.*, 2006, 1147–1156.

52 Y. Dai, X. Song, Z. Wang, S. Ren, Y. Hou and W. Wu, *Chem. Eng. Sci.*, 2026, **320**, 122566.

53 F. Liu, J. Yu, A. B. Qazi, L. Zhang and X. Liu, *Environ. Sci. Technol.*, 2021, **55**, 1419–1435.

54 L. Qiu, A. D. Phule, S. Wen, X. Zhang, Q. Chen and Z. X. Zhang, *Macromol. Mater. Eng.*, 2021, **306**, 2100096.

55 M. S. Aminuddin, M. A. Bustam, C. Y. Chuah and K. Johari, *Ind. Eng. Chem. Res.*, 2025, **64**, 13489–13511.

56 M. S. Aminuddin, M. A. Bustam and K. Johari, *J. Mol. Liq.*, 2025, **423**, 127002.